Ninth International Conference on Computational Fluid Dynamics (ICCFD9), Istanbul, Turkey, July 11-15, 2016 **ICCFD9-2016-211**

Large Eddy Simulation of Endwall Flows in Low Pressure Turbines

Seyfullah Cay, Dogukan T. Karahan, Ayse G. Gungor

Department of Aerospace Engineering, Istanbul Technical University, Istanbul 34469, Turkey
Corresponding author: cays@itu.edu.tr

Abstract: The development of secondary flow structures on a low pressure turbine (LPT) endwall is investigated using large eddy simulation approach. The accurate and reliable prediction of secondary flow losses arising from turbine endwall has great influence on the determination of LPT efficiency. The computational effort in this study is carried out using the open source computational fluid dynamics software OpenFOAM. Results show the important effects of secondary flow structures on separated region.

Keywords: Large-eddy simulation, low pressure turbine, endwall interaction, secondary flows.

1 Introduction

The secondary flow losses arising from endwall and viscous effects have the most significant effect on aerodynamic losses in a low pressure turbine (LPT). An extensive comprehension of the complex and three dimensional nature of the flow field due to secondary flows is the key for a successful and accurate computational effort.

Secondary flows that occur in an LPT environment have two considerable main structures; horseshoe vortex and passage vortex. The formation mechanism of horseshoe vortices is due to coalescence of the boundary layers on the leading edge blade and the end wall. This interaction leads to the generation of two horseshoe vortices; namely, pressure side leg of horseshoe vortex and suction side leg of horseshoe vortex. As their names imply, these vortices are present on the pressure side and suction side of the blade, respectively. A passage vortex is formed due transverse pressure gradient between consecutive blades [1] and the physical evolution of this structure is as follows; the pressure side leg of horseshoe vortex on a blade's pressure side moves towards the trailing edge of its neighboring blade's suction side. These two vortices rotate in opposite directions [2]. Formation of these vortices either completely eliminate the separation that occurs due to strong adverse pressure gradient on the suction side of the blade, or decrease the separation thickness. Therefore, a stronger pressure side leg of horseshoe vortex creates a stronger passage vortex. Also, these secondary flow structures cause substantial pressure losses on the rotor blade.

Most of the studies on this subject have been conducted experimentally [3, 4, 5, 6, 7] and there are quite few number of numerical studies [8, 9]. These studies propose different models for secondary flow structures. Some of these models are shown in figure 1. The main difference between these models is the interaction between passage vortex and suction side leg of horseshoe vortex.

Figure 1(a) shows the most classical secondary flow model [6]. The passage vortex stems from forces caused by the curvature on uniform flow in the midspan region and forces due to the pressure gradient between adjacent blades in the endwall boundary layer. However, the details regarding to features of the secondary flows were not specifically stated in this model[6]. The model in figure 1(b) shows that the suction side leg of horseshoe vortex stays near the intersection region of blade surface and endwall under the passage vortex [3]. In the third model, as shown in figure 1(c), the suction side leg of horseshoe vortex motion ongoing under the passage vortex on the leading edge side of suction side corner region revolves around passage vortex on the trailing edge side [5]. The model suggested in figure 1(d) shows that suction side leg of horseshoe

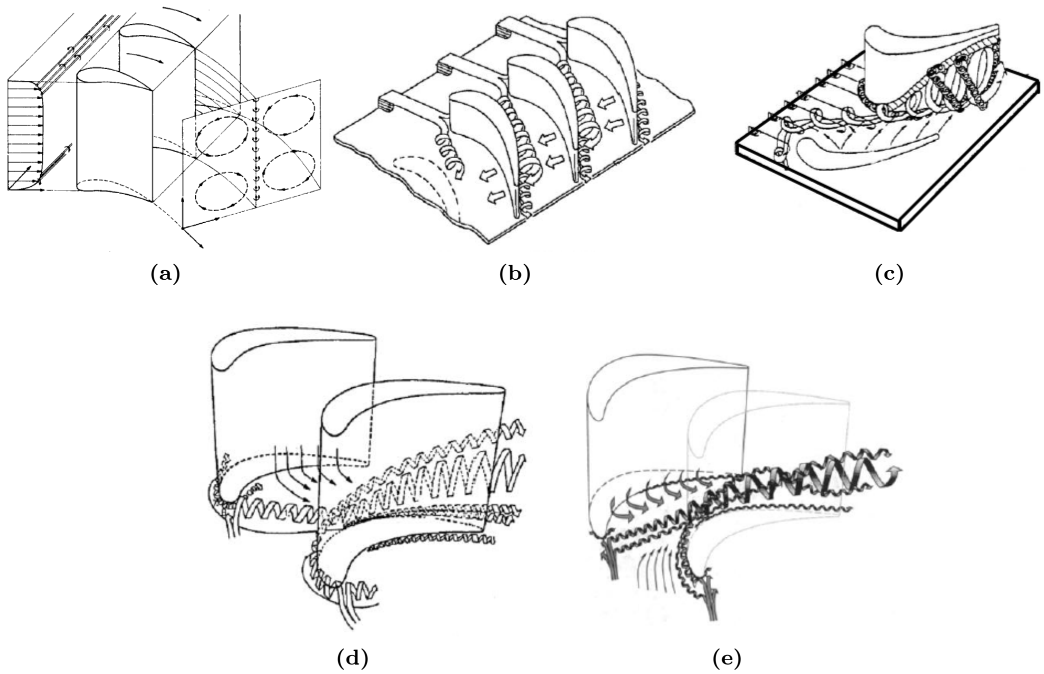

Figure 1: Secondary flow models (a) Hawthorne (1955), (b) Langston (1980), (c) Sharma and Butler (1987), (d) Goldstein and Spores (1988), (e) Wang et al. (1997).

vortex moved on the passage vortex continues towards midspan [4]. The model in the figure 1(e) looks similar to the model shown in figure 1(c), however suction side leg of horseshoe vortex turns once around passage vortex [7]. Understanding the underlying mechanism for secondary flow structures will lead to development of several control strategies. These strategies are particularly important for LPT environments because one can benefit the the alteration of these complex three-dimensional structures so as to reduce the losses and improve the aerodynamic efficiency of the blade.

The objective of this study is twofold; the first one is to investigate the development of secondary flow structures and their influence on the suction side separation bubble and the other one is to provide detailed unsteady flow information to understand the underlying physics of the secondary flow structures. For these purposes, large eddy simulations (LES) of the flow around a T106 turbine blade for different inflow and boundary configurations are presented. This article is subdivided in four parts and these subdivisions cover the mathematical formulation which includes a short description of the numerical method, results, and conclusions, respectively.

2 Mathematical formulation

The effect of end-wall on low pressure turbines for incompressible flows is studied using large eddy simulation approach. LES is currently one of the most promising methods for studying complex flows and it has been successfully applied to many different types of problems.

The governing equations for LES are obtained by applying a spatial filter to Navier-Stokes equations. The spatial filter (acting as a low-pass filter) essentially removes the high wave number contributions. The filtering operation results in the following set of partial differential equations:

$$\frac{\partial \overline{u}_i}{\partial t} + \frac{\partial \overline{u}_i \overline{u}_j}{\partial x_j} = -\frac{1}{\rho}\frac{\partial \overline{p}}{\partial x_i} + \nu \frac{\partial^2 \overline{u}_i}{\partial x_j^2} - \frac{\partial \tau_{ij}^{sgs}}{\partial x_j}; \tag{1}$$

$$\frac{\partial \overline{u}_i}{\partial x_i} = 0; \tag{2}$$

where $\overline{u}_i$ is the filtered velocity field in the x_i direction, and $\overline{p}$ is the filtered pressure field. The spatial filter cannot eradicate the effect of eddies that have high wave numbers (i.e. small eddies or subgrid scale fluctuations) due to presence of the non-linear terms in the momentum equations. The dynamics of these eddies are embedded within the tensor $\tau_{ij}^{sgs} = \overline{u_i u_j} - \overline{u}_i \overline{u}_j$. This tensor is called subgrid scale (sgs) stress tensor. The existence of this tensor results in a closure problem and a model is required in order to close the set of these equations.

The most common method for modeling of τ_{ij}^{sgs} is to assume the following form

$$\tau_{ij}^{sgs} - \frac{\tau_{kk}}{3}\delta_{ij} = -2\nu_t \overline{S}_{ij} \tag{3}$$

where ν_t is the eddy viscosity (which needs to be determined) and $\overline{S}_{ij} = \frac{1}{2}\left(\frac{\partial \overline{u}_i}{\partial x_j} + \frac{\partial \overline{u}_j}{\partial x_i}\right)$ is the resolved strain rate with zero trace.

The Smagorinsky model[10] is the most widely used eddy viscosity model:

$$\nu_\tau = C_s \overline{\Delta}^2 |S|, \quad |S| = 2(\overline{S}_{ij}\overline{S}_{ij})^{1/2} \tag{4}$$

Here, C_s is the Smagorinsky coefficient and $\overline{\Delta}$ is the filter width. This model assumes that there is a balance in the production and dissipation of subgrid kinetic energy. This assumption holds if the subgrid scale field solely represents the dissipative scales of motion. Nevertheless, this is seldom the case in high Reynolds number flows and/or wall bounded turbulence. A remedy to this problem may be supplied by employing a non-equilibrium approach that accounts for the effects of subgrid scale kinetic energy $k^{sgs}\frac{1}{2}(\overline{u_k u_k} - \overline{u_k}\,\overline{u_k})$.

The k-equation model [11] uses such a strategy by relating the sgs kinetic energy to the eddy viscosity with the relation $\nu_\tau = C_\nu \overline{\Delta}\sqrt{k^{sgs}}$. Here, C_ν is a model coefficient that needs to be determined. The subgrid scale kinetic energy field is found by solving the following transport equation:

$$\frac{\partial k^{sgs}}{\partial t} + \frac{\partial \overline{u}_i k^{sgs}}{\partial x_i} = P^{sgs} - D^{sgs} + \frac{\partial}{\partial x_i}(\nu_\tau \frac{\partial k^{sgs}}{\partial x_i}); \tag{5}$$

where $P^{sgs} = -\tau_{ij}^{sgs}\frac{\partial \overline{u}_i}{\partial x_j}$ represents the sgs kinetic energy production, $D^{sgs} = C_\epsilon (k^{sgs})^{3/2}/\overline{\Delta}$ represents the sgs kinetic energy dissipation. The determination of the model coefficient C_ϵ may be based on a dynamic calculation or turbulence theory. In this study we will evaluate the effect of both subgrid models on secondary flow structures.

3 Numerical Method

The geometry, boundary conditions, and the details of the drid for the endwall flow simulations around a T106 turbine blade are shown in figure 2. No-slip boundary condition is applied to the blade surface and the endwall. Periodic boundary is applied to include the effects of consecutive blades on the flow field. Therefore, we have generated a linear cascade and we have omitted the effect of rotation. Table 1 presents the geometrical details of the T106 blade. The reference inlet velocity angle with respect to horizontal direction

Chord	198	$[mm]$
Axial chord	170	$[mm]$
Blade stagger	30.7	$[°]$
Pitch	158	$[mm]$
Span	200	$[mm]$
Inlet flow angle	37.7	$[°]$
Design exit flow angle	63.2	$[°]$

Table 1: T106 blade specifications.

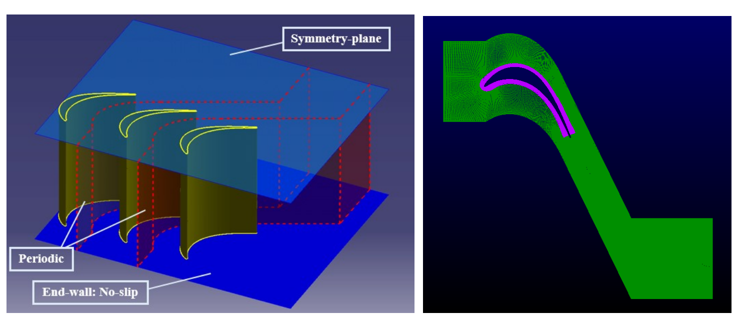

Figure 2: Geometry, boundary conditions, and details of the mesh.

is 37.7°. The Reynolds number based on the inflow velocity, blade chord length, and kinematic viscosity is 8×10^4. The span of the blade is taken to be 100 mm but a blade having a span of 200 mm is represented since domain is assumed to be symmetric with respect to the plane opposing the endall. By employing such an approach, other types of secondary flows (tip vortices, for example) but investigation of these is beyond the scope of this study. In the construction of the computational domain, structured hexahedral elements are employed and the total number of grid points is approximately 3 million.

The computational effort is carried out by using open source computational fluid dynamics software OpenFOAM. The PISO (pressure implicit with splitting of operators) algorithm is used to simulate unsteady, incompressible turbulent flow. The discretization schemes are of second order. A constant time step for which Courent number is less than 1 is set for all cases. The Smagorinsky and k-equation models are used as subgrid scale stress models. The effect of freestream turbulence intensity, Tu, on secondary flow structures is studied by using three different turbulence levels (uniform inflow, 2%, and 5%). Statistics are accumulated for 6 flow-through-times (FTT) after an initial transient of 2 FTT.

4 Results

The end-wall interaction for an untapered, a non-twisted, non-rotating LPT T106 blade will be investigated. In the following subsection, the predictive ability of OpenFOAM in LPT type flows is investigated for the cases that do not involve endwall and freestream turbulence intensity. Then the endwall is introduced in the flow field and the effects of the endwall are discussed in a statistical sense. Sec. 4.2 discusses the secondary flow structures by visual assessment of the flow field. Finally, the last subsection presents effects of inflow turbulence and subgrid scale stress models on secondary flow structures.

4.1 LES of T106 blade with and without endwall

Figure 3 (a) presents the wall static pressure coefficient, calculated based on a reference pressure and dynamic pressure at the inlet plane, along the streamwise direction normalized by the axial chord length, C_{ax}, for the simulations without an endwall (spanwise boundaries are taken to be periodic to simulate an infinitely wide blade). The results for Smagrinsky and k-eqn models and these results are compared with the experimental and DNS data of [?]. The agreement is excellent on both pressure and suction side of the blade. However, there is a slight deviation from the experimental and DNS data near the trailing edge on suction side. This is due to differences in the boundary conditions in experiments and DNS. Figure 3 (b) shows the time-averaged separation region on the suction side of the turbine blade. The formation of two-dimensional separation bubble due to strong adverse pressure gradient caused by the curvature of the blade is at $0.76C_{ax}$. The flow reattaches near the trailing edge.

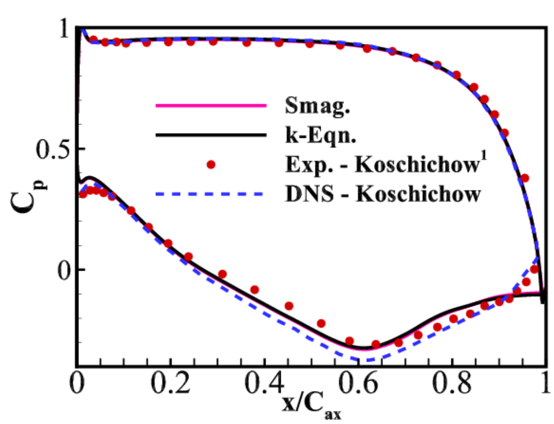

(a)

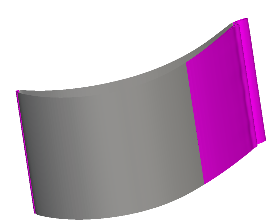

(b)

Figure 3: LES simulations without endwall (a) Wall static pressure coefficient. (b) Separation region predicted with Smagorinsky model.

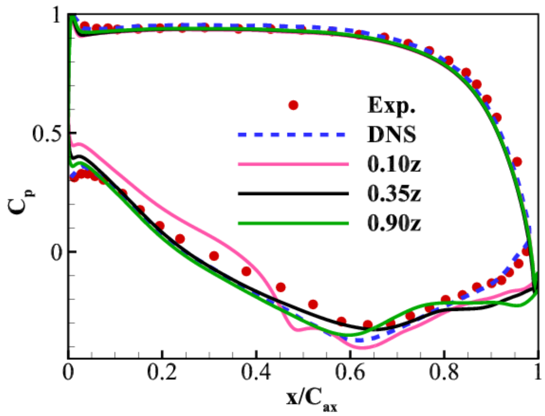

(a)

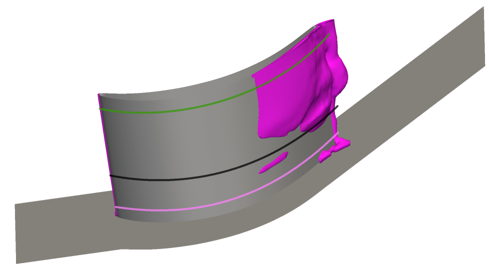

(b)

Figure 4: LES simulations with endwall (a) Wall static pressure coefficient. (b) Separation region predicted with Smagorinsky model.

The effect of endwall on wall static pressure coefficient is depicted in figure 4(a) for three cross sectional planes along the span, very close to the end wall, $0.10z$ plane, slightly far away from the endwall, $0.35z$ plane, and close to the midspan, $0.90z$ plane. Here, z corresponds to the spanwise length simulated. Note that there is no ambiguity in denoting the midspan by $0.90z$. Since the flow is taken to be symmetric with respect to the plane opposing the endwall, $0.90z$ denotion corresponds to the midspan of the whole geometry. The same argument applies to the denotion of the plane $0.35z$. The reader should be aware of this usage. The time-averaged separation region is presented in figure 4(b). These results are obtained using the Smagorinsky model and the freestream turbulence intensity is zero.

At $0.10z$ plane, in the immediate neighborhood of the tip of the blade on the suction side, there is a pressure loss. This pressure loss is a direct result of the formation of the boundary layer on the endwall. The pressure loss increases along the favourable pressure gradient region on the suction side whereas the strength of adverse pressure gradient decreases near endwall due to passage vortex. As a result of this, separation is eliminated by passage vortex close to the endwall, as can be seen in figure 4(b). The pressure loss decreases away from the endwall at the leading edge since the effect of secondary flows on pressure distribution towards midspan decreases. However, the effects of these structures on pressure distribution continue towards midspan due to increment in flow motion from pressure side of adjacent blade to suction side which is caused by transverse pressure gradient. Consequently, the cross-flow separation occurs earlier at around $0.70C_{ax}$ in comparison with the simulation without endwall. Results indicate that separation is eliminated by secondary flows close to the endwall region. Also separation bubble becomes three-dimensional, varies along the span and has different thickness in different parts of separation region due to the effects of secondary flow structures on pressure distribution.

Figure 5 shows the midspan separation region for simulations with and without endwall. Separation starting point and thickness are different because of the secondary flows in the endwall study. The separation starting point is approximately 0.70 axial chord length for the analysis with endwall. However, separation starts nearly 0.76 axial chord length for the analysis without endwall. Therefore our results indicate that the secondary flow structures moves the separation starting point towards the leading edge. Also the reattachment point disappears in the analysis with endwall. So, all of these results indicate that the secondary flows are a loss mechanism in an LPT environment.

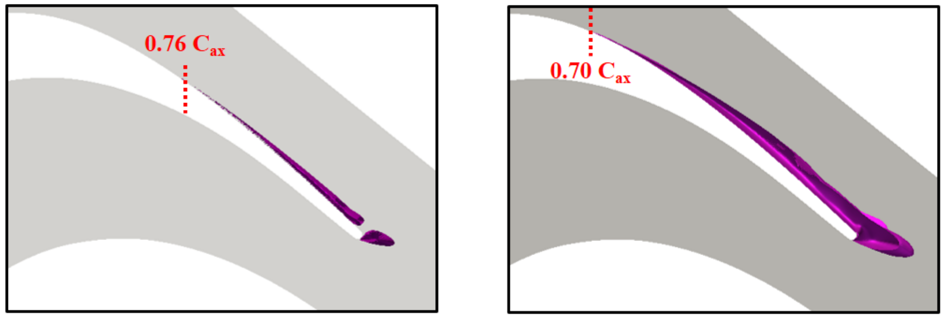

(a) **(b)**

Figure 5: Suction side separation region. (a) Without endwall and (b) With endwall.

4.2 Secondary flow structures

Secondary flows are known to be a loss mechanism for the turbines. These structures are generated as a results of the curvature, endwall boundary layer, and transverse pressure gradient, which is the pressure difference from pressure side towards suction side. When endwall boundary layer encounters with blade surface, streamlines or flow field starts to rotate due to curvature and pressure difference between suction side and adjacent blade pressure side. This rotating flow structures is called secondary flow structures which are produced due to the endwall and viscous effects. There are several secondary flow structures. However, passage vortex and horseshoe vortex are the two main vortices [12].

Figure 6 shows the isosurface of the second invariant of the velocity gradient tensor colored by the spanwise velocity. Horseshoe vortex separates into two legs at the leading edge stagnation point. These legs are pressure side leg and suction side leg of horseshoe vortex. While suction side leg of horseshoe vortex remains near suction side of turbine blades, pressure side leg of horseshoe vortex moves towards adjacent blade pressure side. Then, pressure side leg of horseshoe vortex becomes passage vortex. Therefore, strong pressure side leg of horseshoe vortex creates strong passage vortex. However, these structures cause losses of aerodynamic forces occurring on rotor blades. In order to decrease these losses, the secondary flow structures must be weakened or prevented.

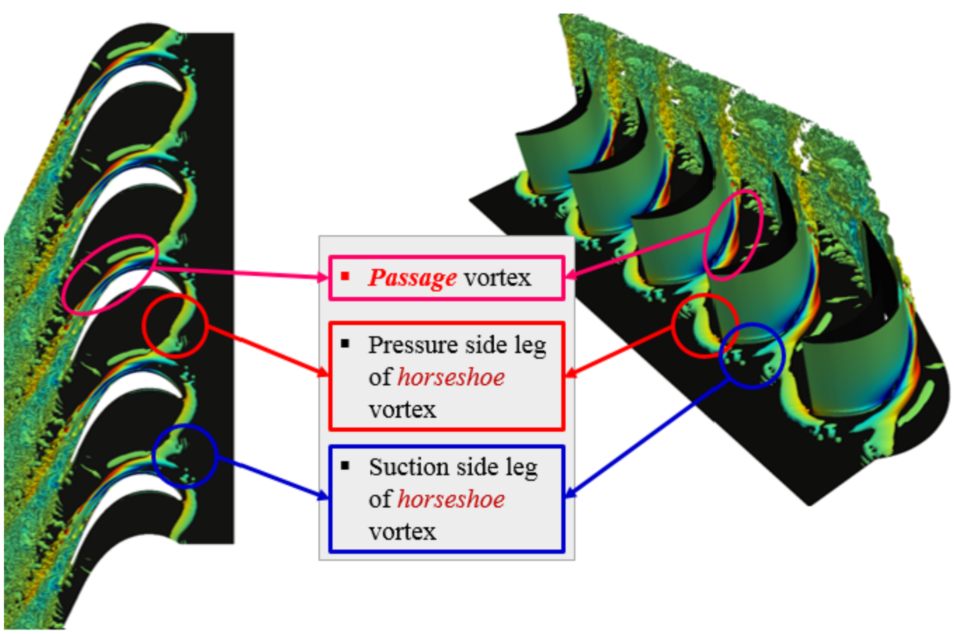

Figure 6: The isosurface of the second invariant of the velocity gradient tensor colored by the spanwise velocity.

The secondary flows, streamlines close to the near endwall region, and separated region (colored by magenta) are presented in figure 7. It is apparent the passage vortex and streamlines overlap each other. Due to high levels of vortical activity downstream, 7(a) cannot provide detailed information about the behaviour of the passage vortex near this region. However, streamlines show that the activity of passage vortex is mostly confined near. This explains the absence of the separation near the endwall. Furthermore, the effect of passage vortex is still present near the midspan as depicted by the streamlines and this results in the alteration of reattachment point.

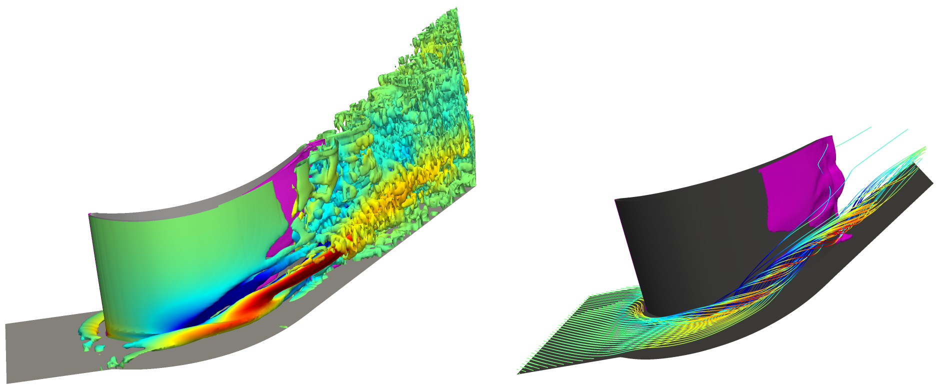

(a) **(b)**

Figure 7: Secondary flow structures. (a) Passage vortex (a) Streamlines.

4.3 Turbulence intensity and subgrid model effect

Since the real turbine blades are subjected to noisy flow field at the inlet plane, it is crucial to introduce some turbulent activity on this plane and discuss their effects on the flow field. No substantial impact on the separation behavior and the pressure distribution along the blade is observed; hence, in this subsection, we will study the effect of inflow turbulence intensity in an instantaneous sense by visualizing the secondary flow structures. Figure 8(a), (b), and (c) present the isosurface of the second invariant of the velocity gradient tensor colored by the spanwise velocity for Smagorinsky model with uniform inlet, $2\%Tu$, and $5\%Tu$, respectively. It is clear that higher levels of turbulent activity at the inlet plane lead to very small changes on secondary flow structures in comparison with results that have uniform inlet condition. Turbulent activity at the inlet plane is apparent at the inlet plane if Tu is increased. Nevertheless, these activities are damped long before flow particles reach the blade. The reason for this is the excessively dissipative behaviour of Smagorinsky model for wall bounded flow. Hence, we extend our analysis by employing k-equation model as a sgs tensor model.

The effect of subgrid model on turbulence and secondary flow structures is clear in figures 8(c) and (d) in which the secondary flow structures are visualised for the Smagorinsky study and k-eqn study, respectively. Both simulations have the same turbulent intensity. Smagorinsky model gives more dissipative and smooth results in comparison with the k-equation model. k-equation model captures the initial turbulence activity. This model has successively sustained the turbulent activity along the way from the inlet to the blade tip and turbulent activity is present all over the blade as seen from the contorted regions colored with mainly green and blue. Results indicate that the subgrid model affects the formation and shape of secondary flow structures considerably.

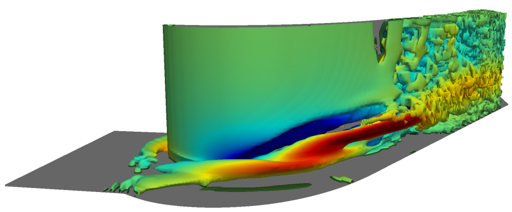

(a)

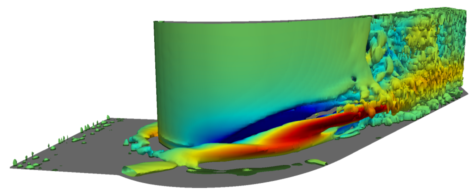

(b)

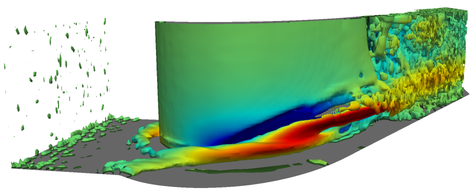

(c)

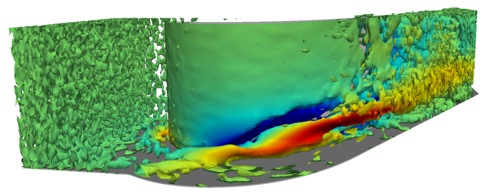

(d)

Figure 8: Turbulence intensity and subgrid model effects. The isosurface of the second invariant of the velocity gradient tensor colored by the spanwise velocity. (a) Smagorinsky model, uniform inlet (b) Smagorinsky model, 2% Tu (c) Smagorinsky model, 5% Tu (d) k-equation model, 5% Tu.

5 Conclusion

The secondary flow structures is investigated by means of large eddy simulation using OpenFOAM. We have mainly focused on two aspects of the endwall flow: details of the secondary flow structures are presented and subsequently some insight is provided into their effect on separation and pressure coefficient. Results have provided crucial insights into the underlying mechanism for endwall induced secondary flow structures. Secondary flow structures eliminate the separation region close to the endwall. However, the thickness of the bubble increased significantly around the midspan and resulted in an increased pressure loss. In order to decrease these losses, the strength secondary flow structures must be weakened or prevented. Turbulence intensity effect appears to be negligible for the Smagorinsky model whereas results obtained with the k-eqn model show significant turbulence activity and change in structural appearance of the secondary flow structures.

References

[1] D. Knezevici. *Controlling secondary flows in very highly-loaded low-pressure turbine cascades.* PhD thesis, Carleton University, 2011.

[2] H. Sauer, R. Muller, and K. Vogeler. Reduction of secondary flow losses in turbine cascades by leading edge modifications at the endwall. *Journal of Turbomachinery*, 123:207–213, 2001.

[3] L.S. Langston. Crossflows in a turbine cascade passage. *Journal of Engineering for Power*, 102:866–874, 1980.

[4] R.J. Goldstein and R.A. Spores. Turbulent transport on the endwall in the region between adjacent turbine blades. *Journal of Heat Transfer*, 110:862–869, 1988.

[5] O.P. Sharma and T.L. Butler. Predictions of endwall losses and secondary flows in axial flow turbine cascades. *Journal of Turbomachinery*, 109:229–236, 1987.

[6] W.R. Hawthorne. Rotational flow through cascades. *Journal of Mechanics and Applied Mathematics*, 3:266–292, 1955.

[7] H.P. Wang, S.J. Olson, R.J. Goldstein, and E.R.G. Eckert. Flow visualization in a linear turbine cascade of high performance turbine blades. *Journal of Turbomachinery*, 119:1–8, 1997.

[8] N. Arndt. Blade row interaction in a multistage low-pressure turbine. *Journal of Turbomachinery*, 115:137–146, 1993.

[9] J. Schlienger, A. I. Kalfas, and R.S. Abhari. Vortex-wake-blade interaction in a shrouded axial turbine. *Journal of Turbomachinery*, 127:699–707, 2005.

[10] J. Smagorinsky. General circulation experiments with the primitive equations. *Monthly Weather Review*, 91:99–164, 1963.

[11] S. Menon, P.K. Yeung, and W.W. Kim. General circulation experiments with the primitive equations. *Computers and Fluids*, 25:165–186, 1996.

[12] J.E. Stephens. *Control of the Tip-Gap Flow of a Low Pressure Turbine Blade in a Linear Cascade*. PhD thesis, University of Notre Dame, 2009.